

## MODAL SPRING REVERB BASED ON DISCRETISATION OF THE THIN HELICAL SPRING MODEL

Jacob McQuillan

Sonic Arts Research Centre  
School of Arts, English and Languages  
Queen's University Belfast, UK  
jmcquillan15@qub.ac.uk

Maarten van Walstijn

Sonic Arts Research Centre  
School of Electronics, Electrical Engineering and Computer Science  
Queen's University Belfast, UK  
m.vanwalstijn@qub.ac.uk

### ABSTRACT

The distributed nature of coupling in helical springs presents specific challenges in obtaining efficient computational structures for accurate spring reverb simulation. For direct simulation approaches, such as finite-difference methods, this is typically manifested in significant numerical dispersion within the hearing range. Building on a recent study of a simpler spring model, this paper presents an alternative discretisation approach that employs higher-order spatial approximations and applies centred stencils at the boundaries to address the underlying linear-system eigenvalue problem. Temporal discretisation is then applied to the resultant uncoupled mode system, rendering an efficient and flexible modal reverb structure. Through dispersion analysis it is shown that numerical dispersion errors can be kept extremely small across the hearing range for a relatively low number of system nodes. Analysis of an impulse response simulated using model parameters calculated from a measured spring geometry confirms that the model captures an enhanced set of spring characteristics.

### 1. INTRODUCTION

Spring reverb is an electromechanical effect originally designed for the Hammond organ to provide a compact form of reverberation [1]. The development of smaller spring reverb tanks in the 1960s facilitated their integration into guitar amplifiers, popularising the effect [2]. The unique sonic qualities due to the complex nature of helical spring vibrations pushed the effect to the mainstream, seeing much success in pop/rock music. Primarily motivated by the modern predominance of digital workflows in audio, several methodologies for spring reverb simulation have emerged (for a recent overview we refer to [3]). One approach uses an efficient computational structure featuring delay and all-pass units to recreate impulse responses, generating reasonably good matches to measurements and allowing parametric control [4, 5, 6, 7]. Another approach works with modal structures that allow enhanced control through direct access to modal parameters [8, 9].

An altogether different class of techniques starts from a physical model in the form of coupled partial differential equations (PDEs), obtaining a finite-difference (FD) scheme via discretisation in time and space. One starting point is the formulation in [10], which neglects the effect of the helix angle. Energy-stable schemes for the simulation of this system have been developed, both with and without magnetic beads [11, 12]. A more complex model,

Copyright: © 2021 Jacob McQuillan et al. This is an open-access article distributed under the terms of the Creative Commons Attribution 3.0 Unported License, which permits unrestricted use, distribution, and reproduction in any medium, provided the original author and source are credited.

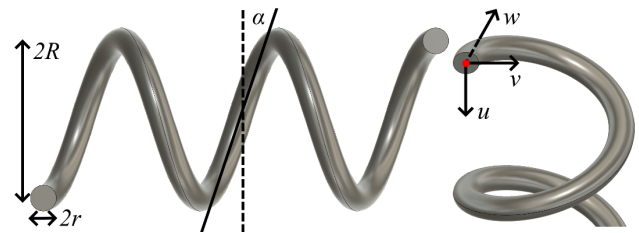


Figure 1: Left: Helical spring side view showing wire radius  $r$  (mm), coil radius  $R$  (mm), and helix angle  $\alpha$ . Right: Orthogonal helical spring polarisations showing longitudinal  $w$ , and transverse  $u$  and  $v$ .

due to Wittrick [13] and featuring twelve variables, incorporates the helix angle (see Figure 1). A ‘thin’ version of this model, which removes two negligible coupling terms, has been derived by Bilbao and Parker [14], and several FD schemes have been proposed [14, 15].

A more recent paper applies higher-order difference approximations to the simpler spring model in [10, 11] and subsequently diagonalises the system to render an efficient modal structure [3]. The main advantage of this approach is that it introduces less numerical error in comparison to the aforementioned FD schemes.

The central aim of the current paper is to apply a similar approach to the more complex spring model. Section 2 re-derives a two-variable version of the thin helical spring model [14, 15], now directly incorporating driving terms and formulating a reciprocal pick-up mechanism. Also, pinned boundary conditions are specified in the two variables. These model choices are loosely based on considerations of how the magnetic beads at either end of the system interact with the spring.

Figure 2 visualises the remainder of the modelling process. A semi-discrete FD scheme with an adjustable spatial stencil width is derived in Section 3. The system is then diagonalised to obtain a set of uncoupled ordinary differential equations (ODEs) in Section 4, after which frequency-dependent damping is imposed. In the final stage, the ODEs are discretised in time with exact preservation of modal frequencies and decay rates.

### 2. HELICAL SPRING MODEL

The physical parameters in the model equations that follow are:  $E$  the Young’s modulus (Pa),  $G$  the shear modulus (Pa),  $A$  the cross-sectional area ( $\text{m}^2$ ),  $\gamma^*$  the shear area correction,  $I$  the transverse moments of inertia ( $\text{m}^4$ ),  $I_\phi$  the polar moments of inertia ( $\text{m}^4$ ),  $\rho$  the material density ( $\text{kg}/\text{m}^3$ ), and  $\kappa = \cos^2(\alpha)/R$  the helix

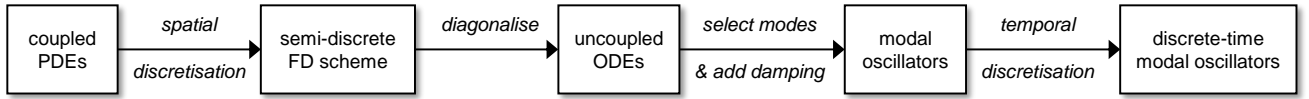


Figure 2: Overview of the modelling process to obtain a modal reverberator from the original set of PDEs describing helical spring vibrations.

curvature ( $\text{m}^{-1}$ ). The full helical spring equations are then written in terms of time  $t$  and curved spatial coordinate  $s$  along the wire axis as

$$\partial_s \xi = \kappa \mathbf{J} \xi + \mathbf{H} \theta + \frac{1}{GA\gamma^*} \mathbf{K} \mathbf{p}, \quad (1)$$

$$\partial_s \theta = \kappa \mathbf{J} \theta + \frac{1}{EI} \mathbf{L} \mathbf{m}, \quad (2)$$

$$\partial_s \mathbf{m} = \kappa \mathbf{J} \mathbf{m} + \mathbf{H} \mathbf{p} + \rho I M \partial_t^2 \theta - \mathbf{g} \mathcal{F}_E, \quad (3)$$

$$\partial_s \mathbf{p} = \kappa \mathbf{J} \mathbf{p} + \rho A \partial_t^2 \xi - \mathbf{g} \mathcal{F}_E, \quad (4)$$

with additional forcing terms to accelerate the relevant components — namely, the last terms in (3) and (4). The choice to excite the system in this form is motivated by the underlying assumption made in [3] that in a real spring tank the electromagnetic field drives the magnetic beads mainly in terms of rotation. In the current model, this loosely translates to exciting the displacement and rotation in the  $u$  polarisation (see Figure 1 for the orientation of the variables). Displacements, rotation angles, moments, and forces are defined, respectively, as

$$\xi = \begin{bmatrix} u \\ v \\ w \end{bmatrix}, \quad \theta = \begin{bmatrix} \theta_u \\ \theta_v \\ \theta_w \end{bmatrix}, \quad \mathbf{m} = \begin{bmatrix} m_u \\ m_v \\ m_w \end{bmatrix}, \quad \mathbf{p} = \begin{bmatrix} p_u \\ p_v \\ p_w \end{bmatrix}, \quad (5)$$

and the operators  $\partial_s^n$  and  $\partial_t^n$  represent  $n^{\text{th}}$  order differentiation with respect to space and time.

Full expansion of (1–4) yields the familiar form of Wittrick’s twelve equations [13]. For a spring of circular cross-section, we have  $\gamma^* = 0.88$ ,  $I = (\pi r^4)/4$ , and  $I_\phi = 2I$  [15], and using the definitions  $\mu = \tan(\alpha)$  and  $b = (EI)/(GI_\phi)$ , the matrices and vector in (1–4) can be specified as

$$\mathbf{J} = \begin{bmatrix} 0 & \mu & -1 \\ -\mu & 0 & 0 \\ 1 & 0 & 0 \end{bmatrix}, \quad \mathbf{H} = \begin{bmatrix} 0 & 1 & 0 \\ -1 & 0 & 0 \\ 0 & 0 & 0 \end{bmatrix}, \quad \mathbf{K} = \begin{bmatrix} 1 & 0 & 0 \\ 0 & 1 & 0 \\ 0 & 0 & \frac{G\gamma^*}{E} \end{bmatrix},$$

$$\mathbf{L} = \begin{bmatrix} 1 & 0 & 0 \\ 0 & 1 & 0 \\ 0 & 0 & b \end{bmatrix}, \quad \mathbf{M} = \begin{bmatrix} 1 & 0 & 0 \\ 0 & 1 & 0 \\ 0 & 0 & \frac{I_\phi}{I} \end{bmatrix}, \quad \mathbf{g} = \begin{bmatrix} 1 \\ 0 \\ 0 \end{bmatrix}. \quad (6)$$

## 2.1. Excitation Torque Distribution

A driving torque  $T_E(t)$  due to electromagnetic forces on the magnet is assumed to translate at the input end to spring torque density  $\mathcal{T}_E(s, t)$  and force density  $\mathcal{F}_E(s, t)$  as

$$\mathcal{T}_E(s, t) = \sin(\phi_E) \psi_E(s) T_E(t), \quad (7)$$

$$\mathcal{F}_E(s, t) = \cos(\phi_E) \psi_E(s) \kappa T_E(t), \quad (8)$$

where the parameter  $\phi_E$  determines the balance between the linear and rotational excitation components and  $\psi_E(s)$  is a distribution function with properties similar to a Dirac delta function:

$$\psi_E(s) = \lim_{\eta \rightarrow 0} \begin{cases} \frac{1}{\eta} & : 0 < s \leq \eta \\ 0 & : s > \eta \end{cases}. \quad (9)$$

## 2.2. Reduced Non-Dimensional Model

A scaled form of the model can be derived using the space and time non-dimensionalisation constants [14, 15]:

$$s_0 = \frac{1}{\kappa}, \quad t_0 = \frac{1}{\kappa^2} \sqrt{\frac{\rho A}{EI}}. \quad (10)$$

These constants are applied to the system as

$$s' = \frac{s}{s_0}, \quad t' = \frac{t}{t_0}, \quad \xi' = \frac{\xi}{s_0}, \quad \mathbf{m}' = \frac{s_0 \mathbf{m}}{EI}, \quad \mathbf{p}' = \frac{s_0^2 \mathbf{p}}{EI},$$

$$T'_E = \frac{s_0 T_E}{EI}, \quad \mathcal{T}'_E = \frac{s_0^2 \mathcal{T}_E}{EI}, \quad \mathcal{F}'_E = \frac{s_0^3 \mathcal{F}_E}{EI}, \quad (11)$$

where prime symbols indicate a non-dimensional term. After (11), the prime symbols are removed for readability. The unwound spring length  $L$  (m) is also defined and non-dimensionalised as  $\lambda = L/s_0$ .

Wittrick’s model [13] describes helical spring vibrations generally, and typical springs found in spring reverb tanks are thin. Thus, factors proportional to  $r^2/R^2$  are very small and may be neglected [14, 15] — namely, the last term in (1) and the penultimate term in (3) after non-dimensionalisation of the system. The resultant thin spring model with the added excitation terms is written as

$$\partial_s \xi = \mathbf{J} \xi + \mathbf{H} \theta, \quad \partial_s \mathbf{m} = \mathbf{J} \mathbf{m} + \mathbf{H} \mathbf{p} - \mathbf{g} \mathcal{T}_E,$$

$$\partial_s \theta = \mathbf{J} \theta + \mathbf{L} \mathbf{m}, \quad \partial_s \mathbf{p} = \mathbf{J} \mathbf{p} + \partial_t^2 \xi - \mathbf{g} \mathcal{F}_E. \quad (12)$$

Figure 2 in [15] shows that this simplification does not alter vibrations in the audio range. Following a similar approach as taken in [14, 15], the model is reduced to a system in only 8 variables:

$$\tilde{\theta} = \mathbf{Q} \tilde{\xi}, \quad \tilde{\mathbf{p}} = \mathbf{Q} \tilde{\mathbf{m}} + \chi_1 \mathcal{T}_E,$$

$$\mathbf{D} \tilde{\mathbf{m}} = \mathbf{Q}^* \tilde{\theta}, \quad \mathbf{A} \partial_t^2 \tilde{\xi} = \mathbf{Q}^* \tilde{\mathbf{p}} + \chi_2 \mathcal{F}_E. \quad (13)$$

The reduced variables are composed of the original displacements, rotation angles, moments, and forces, respectively, as

$$\tilde{\xi} = \begin{bmatrix} v \\ w \end{bmatrix}, \quad \tilde{\theta} = \begin{bmatrix} \theta_u \\ \theta_v \end{bmatrix}, \quad \tilde{\mathbf{m}} = \begin{bmatrix} m_v \\ m_w \end{bmatrix}, \quad \tilde{\mathbf{p}} = \begin{bmatrix} p_u \\ p_v \end{bmatrix}, \quad (14)$$

and the reduced model in (13) makes use of matrices and vectors holding differential operators:

$$\mathbf{Q} = \begin{bmatrix} -\partial_s & -\mu \partial_s \\ -\mu & 1 + \partial_s^2 \end{bmatrix}, \quad \mathbf{Q}^* = \begin{bmatrix} \mu & \partial_s \\ -1 - \partial_s^2 & \mu \partial_s \end{bmatrix}, \quad \chi_1 = \begin{bmatrix} 0 \\ 1 \end{bmatrix}, \quad (15)$$

$$\mathbf{A} = \begin{bmatrix} 1 & 0 \\ 0 & 1 - \partial_s^2 \end{bmatrix}, \quad \mathbf{D} = \begin{bmatrix} 1 & 0 \\ 0 & b - \partial_s^2 \end{bmatrix}, \quad \chi_2 = \begin{bmatrix} 0 \\ -\partial_s \end{bmatrix}. \quad (16)$$

The final reduction yields a system in only  $\tilde{\xi}$  [14, 15], here with the accelerations written explicitly as

$$\partial_t^2 \tilde{\xi} = \partial_s^2 \mathbf{A}^{-1} \mathbf{R} \mathbf{D}^{-1} \mathbf{R} \tilde{\xi} + \mathbf{A}^{-1} \mathbf{Q}^* \chi_1 \mathcal{T}_E + \mathbf{A}^{-1} \chi_2 \mathcal{F}_E, \quad (17)$$

which uses the new matrix differential operator  $\mathbf{R}$ :

$$\partial_s \mathbf{R} = \mathbf{Q}^* \mathbf{Q}, \quad \mathbf{R} = \begin{bmatrix} -2\mu & 1 - \mu^2 + \partial_s^2 \\ 1 - \mu^2 + \partial_s^2 & 2\mu(1 + \partial_s^2) \end{bmatrix}. \quad (18)$$

Consolidating the matrices and vectors relating to the excitation

$$\mathbf{z}_E = \sin(\phi_E) \mathbf{A}^{-1} \mathbf{Q}^* \boldsymbol{\chi}_1 + \cos(\phi_E) \mathbf{A}^{-1} \boldsymbol{\chi}_2 = [z_{vE} \ z_{wE}]^T, \quad (19)$$

allows writing the model in expanded form as

$$\begin{aligned} \partial_t^2 v &= z_1 v + z_2 w + \gamma_{vE} T_E, \\ \partial_t^2 w &= z_3 v + z_4 w + \gamma_{wE} T_E. \end{aligned} \quad (20)$$

The  $z_1$ - $z_4$  operators are

$$z_1 = 4\mu^2 \partial_s^2 + \left( \frac{\partial_s^2 (1 - \mu^2 + \partial_s^2)^2}{b - \partial_s^2} \right), \quad (21)$$

$$\begin{aligned} z_2 &= -2\mu \partial_s^2 (1 - \mu^2 + \partial_s^2) \\ &+ \left( \frac{\partial_s^2 (1 - \mu^2 + \partial_s^2) (2\mu + 2\mu \partial_s^2)}{b - \partial_s^2} \right), \end{aligned} \quad (22)$$

$$\begin{aligned} z_3 &= \left( \frac{-2\mu \partial_s^2 (1 - \mu^2 + \partial_s^2)}{1 - \partial_s^2} \right) \\ &+ \left( \frac{\partial_s^2 (1 - \mu^2 + \partial_s^2) (2\mu + 2\mu \partial_s^2)}{(b - \partial_s^2) (1 - \partial_s^2)} \right), \end{aligned} \quad (23)$$

$$z_4 = \left( \frac{\partial_s^2 (1 - \mu^2 + \partial_s^2)^2}{1 - \partial_s^2} \right) + \left( \frac{\partial_s^2 (2\mu + 2\mu \partial_s^2)^2}{(b - \partial_s^2) (1 - \partial_s^2)} \right), \quad (24)$$

and the excitation terms are

$$\gamma_{vE}(s) = z_{vE} \psi_E(s) = \sin(\phi_E) \partial_s \psi_E(s), \quad (25)$$

$$\gamma_{wE}(s) = z_{wE} \psi_E(s) = [-\cos(\phi_E) + \mu \sin(\phi_E)] \frac{\partial_s}{1 - \partial_s^2} \psi_E(s), \quad (26)$$

where the inverse differential operators are denoted with divisions in (21-26), e.g.

$$\frac{\partial_s}{1 - \partial_s^2} v := (1 - \partial_s^2)^{-1} \partial_s v. \quad (27)$$

### 2.3. Pick-Up

Obtaining an output using a reciprocal mechanism can be achieved by collecting torque density and force density over a similarly weighted range as for the input at the other end of the spring. Hence, following the definitions in Section 2.1, we can specify  $\psi_P(s) = \psi_E(1 - s)$ , and the output can be defined initially in terms of  $\partial_t^2 \theta_u$  and  $\partial_t^2 u$ . Using the relationships in (12), and considering non-dimensional force density and torque density are both formulated from the torque in (7,8), an output can then be written in terms of the reduced model variables  $v$  and  $w$ :

$$\begin{aligned} T_P(t) &= \int_0^\lambda \psi_P(s) \{ \cos(\phi_P) \partial_t^2 u + \sin(\phi_P) \partial_t^2 \theta_u \} ds, \\ &= \int_0^\lambda \psi_P(s) \left\{ \cos(\phi_P) \partial_s \partial_t^2 w \right. \\ &\quad \left. + \sin(\phi_P) \left( -\partial_s \partial_t^2 v - \mu \partial_s \partial_t^2 w \right) \right\} ds, \\ &= \int_0^\lambda \gamma_{vP}(s) [z_1 v + z_2 w] + \gamma_{wP}(s) [z_3 v + z_4 w] ds, \end{aligned} \quad (28)$$

where

$$\gamma_{vP}(s) = -\sin(\phi_P) \partial_s \psi_P(s), \quad (29)$$

$$\gamma_{wP}(s) = [\cos(\phi_P) - \mu \sin(\phi_P)] \partial_s \psi_P(s), \quad (30)$$

and the parameter  $\phi_P$  determines the balance between the pick-up components. The reduced two-variable model with a defined excitation and pick-up relies only on five parameters:  $b$ ,  $\mu$ ,  $\lambda$ ,  $\phi_E$ , and  $\phi_P$ .

### 2.4. Boundary Conditions

In the derivation of a modal structure, it is useful to systematically ensure that the modes have real-valued frequencies and are thus undamped. One requirement is that the boundary conditions of the continuous-domain model are specified in lossless form, which is ensured when the boundary term

$$\mathcal{B} = p_u \partial_t u + p_v \partial_t v + p_w \partial_t w + m_u \partial_t \theta_u + m_v \partial_t \theta_v + m_w \partial_t \theta_w, \quad (31)$$

derived in [15] via energy analysis is zero at  $s = \{0, \lambda\}$ . This is achieved by at least one of the terms in each of the six products in (31) going to zero, and a large set of different combinations of conditions in the twelve variables satisfies this requirement [15]. One possible case is presented here, setting  $p_u = \partial_t v = \partial_t w = m_u = \partial_t \theta_v = \partial_t \theta_w = 0$ . Under certain assumptions on the continuity of the system's solution,<sup>1</sup> one may employ the thin spring model equations to obtain corresponding conditions for the reduced model variables  $v$  and  $w$ . Continuing from (12), the following relationship is derived:

$$\begin{bmatrix} v \\ w \\ \partial_s^2 v \\ \partial_s^2 w \\ \partial_s^4 v \\ \partial_s^4 w \end{bmatrix} = \begin{bmatrix} 0 & 1 & 0 & 0 & 0 & 0 \\ 0 & 0 & 1 & 0 & 0 & 0 \\ 0 & -\mu^2 & \mu & -1 & -2\mu & 1 \\ 0 & \mu & -1 & 0 & 1 & 0 \\ 4\mu & \Upsilon_1 & \Upsilon_2 & \Upsilon_4 & \Upsilon_5 & \Upsilon_6 \\ -1 & \Upsilon_2 & \Upsilon_3 & -3\mu & \Upsilon_6 & 2\mu \end{bmatrix} \begin{bmatrix} p_u \\ v \\ w \\ m_u \\ \theta_v \\ \theta_w \end{bmatrix}, \quad (32)$$

where

$$\Upsilon_1 = -\partial_t^2 + \mu^4 + \mu^2, \quad \Upsilon_2 = -\mu^3 - \mu, \quad \Upsilon_3 = \mu^2 + 1, \quad (33)$$

$$\Upsilon_4 = 6\mu^2 + b + 2, \quad \Upsilon_5 = 4\mu^3 + 2\mu, \quad \Upsilon_6 = -3\mu^2 - 1. \quad (34)$$

By setting the right-hand vector in (32) to zero, one immediately obtains boundary conditions in  $v$  and  $w$ :

$$\begin{aligned} v(0, t) &= 0, & \partial_s^2 v(0, t) &= 0, & \partial_s^4 v(0, t) &= 0, \\ w(0, t) &= 0, & \partial_s^2 w(0, t) &= 0, & \partial_s^4 w(0, t) &= 0, \end{aligned} \quad (35)$$

$$\begin{aligned} v(\lambda, t) &= 0, & \partial_s^2 v(\lambda, t) &= 0, & \partial_s^4 v(\lambda, t) &= 0, \\ w(\lambda, t) &= 0, & \partial_s^2 w(\lambda, t) &= 0, & \partial_s^4 w(\lambda, t) &= 0, \end{aligned} \quad (36)$$

noting that when  $v$ ,  $w$ ,  $\theta_v$ , and  $\theta_w$  are zero at the endpoints, their time derivatives are also zero at the endpoints.

Furthermore, from (12) one obtains  $u = \partial_s w$  and  $\theta_u = -\partial_s v - \mu \partial_s w$ , meaning that there are corresponding conditions in  $u$  and  $\theta_u$  of the form

$$\partial_s u(0, t) = \partial_s^3 u(0, t) = 0, \quad \partial_s u(\lambda, t) = \partial_s^3 u(\lambda, t) = 0, \quad (37)$$

$$\partial_s \theta_u(0, t) = \partial_s^3 \theta_u(0, t) = 0, \quad \partial_s \theta_u(\lambda, t) = \partial_s^3 \theta_u(\lambda, t) = 0, \quad (38)$$

<sup>1</sup>Such assumptions are common in engineering problems [16] and inherent to the energy analysis underpinning the boundary term in (31).

which demonstrates the useful feature of  $u$  and  $\theta_u$  not being fixed at the endpoints, thus enabling excitation and pick-up at the system's extremes in those variables.

## 2.5. Dispersion Relation

The dispersion relation links the temporal frequency  $\omega$  to the spatial frequency (wavenumber)  $\beta$ . Figure 3 visualises how the incorporation of a helix angle yields two curves in the audio range (see [14] for a detailed analysis of the curves and their various behaviours). The dispersion relation is derived by omitting the

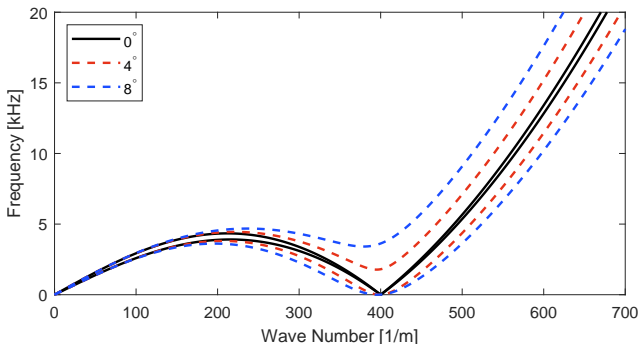


Figure 3: Dispersion relations with varied helix angles.

driving terms and using the ansatz  $e^{j(\omega t + \beta s)}$  to obtain new expressions  $v(s, t) = V e^{j(\omega t + \beta s)}$  and  $w(s, t) = W e^{j(\omega t + \beta s)}$ , where  $V$  and  $W$  represent complex amplitudes. Substitution of the above expressions into (20) and allowing the exponential appearing in all terms to cancel yields the following system:

$$\begin{bmatrix} (\omega^2 + z_1) & z_2 \\ z_3 & (\omega^2 + z_4) \end{bmatrix} \begin{bmatrix} V \\ W \end{bmatrix} = \begin{bmatrix} 0 \\ 0 \end{bmatrix}, \quad (39)$$

where the operators  $z_1$ – $z_4$  from (21–24) transform by substituting  $\partial_s^2$  with  $-\beta^2$ . Non-trivial solutions occur when the determinant of the matrix in (39) is zero:

$$\omega^4 + (z_1 + z_4)\omega^2 + z_1 z_4 - z_2 z_3 = 0, \quad (40)$$

and the frequencies are then obtained directly by solving (40).

## 3. SPATIAL DISCRETISATION

### 3.1. Difference Operators

The number of spatial segments  $M$  can be freely chosen to yield a spatial step  $\Delta_s = (\lambda/M)$ . A semi-discrete representation of  $\tilde{\xi}(s, t)$  is  $\tilde{\xi}(m\Delta_s, t)$ , written compactly as  $\tilde{\xi}_m$ , where  $m$  represents the spatial index. Let the centred difference operator approximating the  $n^{\text{th}}$  spatial derivative be defined as

$$\delta_n^{(K)} v_m = \sum_{k=-K}^K d_{n,k}^{(K)} v_{m+k}, \quad (41)$$

where  $K$  is the number of nodes evaluated on either side of the central node, thus the stencil width is  $2K + 1$ . For discretisation of the continuous system, only the first and second spatial derivative has to be evaluated (as can be seen from (20), higher derivatives result by repeated application of the second derivative operator). The required coefficients can be calculated either in classic

form, e.g. based on Taylor-series approximations [17], or via optimisation (see, e.g. [18]). The latter approach usually minimises an  $L^2$  or  $L^\infty$  norm error in the (spatial) frequency domain, as such offering a more uniform distribution of the approximation error across the relevant wavenumber range. In the current paper this is achieved by first writing the higher-order approximation as

$$n=1: \quad \partial_s v(m\Delta_s) \approx \sum_{k=1}^K a_k \left( \frac{v_{m+k} - v_{m-k}}{2\Delta_s} \right), \quad (42)$$

$$n=2: \quad \partial_s^2 v(m\Delta_s) \approx \sum_{k=1}^K a_k \left( \frac{v_{m+k} - 2v_m + v_{m-k}}{\Delta_s^2} \right). \quad (43)$$

An overdetermined linear system of equations is then formed by setting the difference operator equal to the differentiation operator at an equidistant set of points  $\beta_i = (i\nu)/(2N\Delta_s)$  along the spatial frequency axis, with  $i = 0, 1, 2, \dots, N$ . This can be written as

$$\mathbf{S}\mathbf{a} = \mathbf{1}, \quad (44)$$

where  $\mathbf{a} = [a_1 \ a_2 \ \dots \ a_K]^T$ ,  $\mathbf{1}$  is a column vector of length  $N + 1$  with all elements set to 1, and  $\mathbf{S}$  is an  $(N + 1) \times K$  matrix with elements

$$n=1: \quad S_{i,k} = \frac{\sin(k\beta_i)}{k\beta_i}, \quad (45)$$

$$n=2: \quad S_{i,k} = \left[ \frac{\sin(\frac{1}{2}k\beta_i)}{\frac{1}{2}k\beta_i} \right]^2. \quad (46)$$

The  $L^2$ -optimal coefficients  $a_k$  are found using the pseudo-inverse of  $\mathbf{S}$ , and the coefficients  $d_{2,k}^{(K)}$  are then readily calculated. The factor  $0 < \nu < 1$  determines the wavenumber range to optimise over; here we used  $\nu = 0.9$  and  $N = 1000$ .

### 3.2. Helical Spring

The system in (20) is discretised in space using the difference operator in (41):

$$\begin{aligned} \partial_t^2 v_m &= \bar{z}_1 v_m + \bar{z}_2 w_m + \bar{\gamma}_{vE,m} T_E, \\ \partial_t^2 w_m &= \bar{z}_3 v_m + \bar{z}_4 w_m + \bar{\gamma}_{wE,m} T_E, \end{aligned} \quad (47)$$

where the overbar in  $\bar{z}_1$ – $\bar{z}_4$  is used to denote the discrete-domain representation of the operators.

### 3.3. Boundary Conditions

The boundary conditions in (35,36) must be satisfied in numerical form. A wide stencil applied near the system boundaries implies the necessity to eliminate multiple ghost nodes, i.e. points outside the interior domain. Due to the aforementioned repeated applications of the second derivative operator (as seen in (21–24)), the stencil width becomes  $6K + 1$ . Therefore, for both  $v$  and  $w$ , the number of ghost nodes that must be accounted for on either side of the system is  $P = 3K - 1$ . For the variable  $v$  at  $s = 0$ , and taking into account that  $v_0 = 0$  for pinned conditions, centred approximations to the second and fourth derivatives can be written

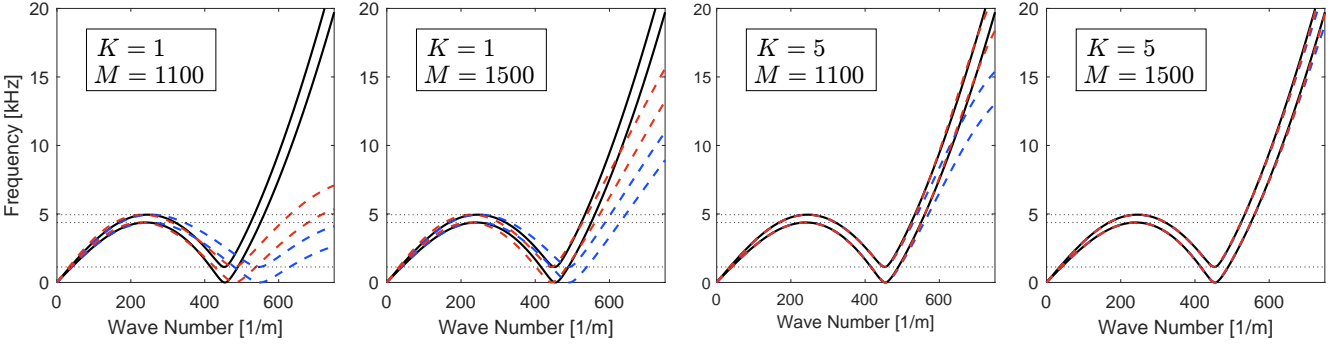


Figure 4: Dispersion curves for spring parameters as given in Table 1. The dotted lines indicate the system's three transition frequencies. Legend: — continuous-domain, - - numerical (classic FD coefficients), - . - numerical (optimised FD coefficients).

numerically as

$$\delta_2^{(P)} v_0 = \sum_{p=-P}^P d_{2,p}^{(P)} v_p = \sum_{p=1}^P d_{2,p}^{(P)} (v_p + v_{-p}), \quad (48)$$

$$\delta_4^{(P)} v_0 = \sum_{p=-P}^P d_{4,p}^{(P)} v_p = \sum_{p=1}^P d_{4,p}^{(P)} (v_p + v_{-p}), \quad (49)$$

where we have made use of the coefficient symmetry property that holds for centred difference approximations of even derivatives. Therefore, if we write all ghost points as mirrored versions of their interior domain counterparts:

$$\text{For } p = 1, 2, 3 \dots P : \quad \begin{cases} v_{-p} = -v_p \\ v_{M-p} = -v_{M+p} \end{cases}, \quad (50)$$

and substitute into (48,49), then it follows that the boundary conditions for  $v$  at  $s = 0$  are satisfied as

$$v_0 = 0, \quad \delta_2^{(P)} v_0 = 0, \quad \delta_4^{(P)} v_0 = 0. \quad (51)$$

Hence, the accuracy with which the two derivative conditions are met is determined by the chosen stencil width. The same methodology is applied at  $s = \lambda$  and for the  $w$  polarisation.

### 3.4. Input and Output

The discrete input torque in (47) is adapted directly from Section 2.1, and the discrete distributions  $\bar{\gamma}_{vE,m}$  and  $\bar{\gamma}_{wE,m}$  are derived from their continuous counterparts in (25,26) as

$$\bar{\gamma}_{vE,m} = \sin(\phi_E) \bar{\zeta}_{E,m}, \quad (52)$$

$$\bar{\gamma}_{wE,m} = [-\cos(\phi_E) + \mu \sin(\phi_E)] \frac{1}{1 - \delta_2^{(K)}} \bar{\zeta}_{E,m}, \quad (53)$$

where  $\bar{\zeta}_{E,m}$  is written as

$$\bar{\zeta}_{E,m} = \begin{cases} 2\delta_1^{(K)} \bar{\psi}_{E,m} & : m = 1, 2, 3 \dots K \\ 0 & : \text{elsewhere} \end{cases}, \quad (54)$$

using the discrete unit impulse function  $\bar{\psi}_{E,m}$  as the discrete-domain counterpart of the distribution function in (9), i.e.  $\bar{\psi}_{E,0} = 1/\Delta_s$ . Here, the symmetries specified in (50) have been applied so that the FD coefficients in  $\bar{\zeta}_{E,m}$  are expressed for  $m = 1, 2, 3 \dots K$ .

The discrete output torque is derived in a similar manner, adapting its continuous counterpart in (28) as

$$T_P = \sum_{m=1}^{M-1} [\bar{\gamma}_{vP,m} (\bar{z}_1 v_m + \bar{z}_2 w_m) + \bar{\gamma}_{wP,m} (\bar{z}_3 v_m + \bar{z}_4 w_m)] \Delta_s, \quad (55)$$

$$\bar{\gamma}_{vP,m} = -\sin(\phi_P) \bar{\zeta}_{P,m}, \quad (56)$$

$$\bar{\gamma}_{wP,m} = [\cos(\phi_P) - \mu \sin(\phi_P)] \bar{\zeta}_{P,m}, \quad (57)$$

where  $\bar{\zeta}_{P,M-m} = -\bar{\zeta}_{E,m}$ , meaning it is non-zero at  $(M - K) \leq m < M$  and zero elsewhere.

### 3.5. Dispersion Analysis

The numerical dispersion curves for the scheme are derived analogous to Section 2.5, now by inserting a similar ansatz  $e^{j(\omega t + \beta m \Delta_s)}$ :

$$v_m = V e^{j(\omega t + \beta m \Delta_s)}, \quad w_m = W e^{j(\omega t + \beta m \Delta_s)}. \quad (58)$$

Figure 4 visualises how the numerical parameters affect the accuracy across the hearing range — namely, the number of spatial segments  $M$ , the FD stencil width  $6K + 1$ , and the choice between classic and optimised FD coefficients. The plot shows how increasing either  $K$  or  $M$  gradually improves the match with the continuous-domain. The optimised FD coefficients provide a good match with  $K = 5$  and  $M = 1100$ , while the classic FD coefficients require a higher  $M$  to obtain high accuracy over a similar range.

Considering the lower significance of frequencies above 17 kHz, it can be concluded that discretisation errors can be made negligibly small across the hearing range, which is an improvement on previous discretisation approaches (e.g. compared to Figures 5 and 10 in [15]). The improved performance of optimised coefficients over the Taylor-series derived coefficients is particularly useful in the pursuit of accurate simulations for larger springs, as a lower number of nodes can be chosen, thus providing more headroom before running into numerical issues in the subsequent modal formulation due to large-matrix eigenvalue computations.

### 3.6. Vector-Matrix Scheme

Deriving a vector-matrix form of the scheme works towards developing an FD coefficients matrix for diagonalisation. The eigenvalues extracted will then be used to derive a modal system. Let's

define  $\mathbf{v}$  and  $\mathbf{w}$  as column vectors holding the interior domain node values for their respective polarisations:

$$\mathbf{v} = [v_1 \ v_2 \ \dots \ v_{M-1}]^T, \quad \mathbf{w} = [w_1 \ w_2 \ \dots \ w_{M-1}]^T. \quad (59)$$

A matrix  $\tilde{\mathbf{D}}_2^{(K)}$  holding all FD weights necessary for the second derivative approximation is constructed as in [3]:

$$\delta_2^{(K)} \mathbf{v} = \tilde{\mathbf{D}}_2^{(K)} \tilde{\mathbf{v}}, \quad (60)$$

where

$$\tilde{\mathbf{v}} = [\mathbf{v}_L^T \ v_0 \ \mathbf{v}^T \ v_M \ \mathbf{v}_R^T]^T, \quad (61)$$

$$\mathbf{v}_L = [v_{-(K-1)} \ v_{-(K-2)} \ \dots \ v_{-2} \ v_{-1}]^T, \quad (62)$$

$$\mathbf{v}_R = [v_{(M+1)} \ v_{(M+2)} \ \dots \ v_{(M+K-2)} \ v_{(M+K-1)}]^T. \quad (63)$$

Ghost nodes outside the domain are included in the formulation, as evident from the vector  $\tilde{\mathbf{v}}$ . See Figure 4 in [3] for a visualisation of the construction of the FD matrix. Partitioning this extended matrix isolates the interior domain and the outer matrix partitions holding the ghost nodes are incorporated using the symmetries specified in (50). This yields a new square matrix  $\mathbf{D}_2^{(K)}$  in (64), of dimensions  $(M-1) \times (M-1)$ , which holds all the FD weights required for calculation within the interior domain:

$$\delta_2^{(K)} \mathbf{v} = \mathbf{D}_2^{(K)} \mathbf{v}, \quad \delta_2^{(K)} \mathbf{w} = \mathbf{D}_2^{(K)} \mathbf{w}. \quad (64)$$

The scheme in (47) can now be written in vector-matrix form. This uses the matrix  $\mathbf{D}_2^{(K)}$  to replace all instances of  $\delta_2^{(K)}$ , i.e. the centred FD approximation to the second spatial derivative, for  $\bar{z}_1 - \bar{z}_4$  in (47):

$$\partial_t^2 \mathbf{x} = \mathbf{Z}\mathbf{x} + \mathbf{h}_E T_E, \quad (65)$$

where

$$\mathbf{x} = \begin{bmatrix} \mathbf{v} \\ \mathbf{w} \end{bmatrix}, \quad \mathbf{Z} = \begin{bmatrix} \mathbf{Z}_1 & \mathbf{Z}_2 \\ \mathbf{Z}_3 & \mathbf{Z}_4 \end{bmatrix}, \quad \mathbf{h}_E = \begin{bmatrix} \tilde{\gamma}_{vE} \\ \tilde{\gamma}_{wE} \end{bmatrix}. \quad (66)$$

The matrix  $\mathbf{Z}_1$  is derived from the operator  $z_1$  in (21) as

$$\mathbf{Z}_1 = 4\mu^2 \mathbf{D}_2^{(K)} + \left( \frac{\mathbf{D}_2^{(K)} (\mathbf{I} - \mu^2 \mathbf{I} + \mathbf{D}_2^{(K)})^2}{b\mathbf{I} - \mathbf{D}_2^{(K)}} \right), \quad (67)$$

which also incorporates the identity matrix  $\mathbf{I}$ , of dimensions  $(M-1) \times (M-1)$ . The matrices  $\mathbf{Z}_2 - \mathbf{Z}_4$  are derived analogous to (67), the column vector  $\tilde{\gamma}_{vE}$  has elements as given by the grid function in (52) for  $m = 1, 2, 3 \dots K$ , and  $\tilde{\gamma}_{wE}$  is derived using both the grid function in (53) and the vector-matrix formulations:

$$\tilde{\gamma}_{wE} = [-\cos(\phi_E) + \mu \sin(\phi_E)] (\mathbf{I} - \mathbf{D}_2^{(K)})^{-1} \bar{\zeta}_E, \quad (68)$$

where the vector  $\bar{\zeta}_E$  is obtained from (54). The consolidated column vectors  $\mathbf{x}$  and  $\mathbf{h}_E$  are of length  $2(M-1)$  and the FD matrix  $\mathbf{Z}$  has dimensions  $2(M-1) \times 2(M-1)$ . For the scheme in (65), the output torque is defined as

$$T_P = \mathbf{h}_P^T \mathbf{Z}\mathbf{x}, \quad \mathbf{h}_P = \begin{bmatrix} \tilde{\gamma}_{vP} \\ \tilde{\gamma}_{wP} \end{bmatrix} \Delta_s, \quad (69)$$

and the column vectors  $\tilde{\gamma}_{vP}$  and  $\tilde{\gamma}_{wP}$  are obtained directly from the grid functions in (56,57).

## 4. MODAL FORMULATION

### 4.1. Diagonalisation

To develop a modal system, the FD matrix  $\mathbf{Z}$  in (65) is diagonalised:

$$\mathbf{Z} = \mathbf{P}\mathbf{Q}\mathbf{P}^{-1}. \quad (70)$$

$\mathbf{Q}$  is diagonal and holds the eigenvalues of  $\mathbf{Z}$ , and  $\mathbf{P}$  holds the corresponding eigenvectors. The expression in (70) is substituted into the vector-matrix scheme in (65), which is then pre-multiplied with  $\mathbf{P}^{-1}$ :

$$\mathbf{P}^{-1} \partial_t^2 \mathbf{x} = \mathbf{Q}\mathbf{P}^{-1} \mathbf{x} + \mathbf{P}^{-1} \mathbf{h}_E T_E. \quad (71)$$

Let  $\mathbf{c}_E = \mathbf{P}^{-1} \mathbf{h}_E$  and  $\mathbf{y} = \mathbf{P}^{-1} \mathbf{x}$ , yielding the following scheme:

$$\partial_t^2 \mathbf{y} = \mathbf{Q}\mathbf{y} + \mathbf{c}_E T_E, \quad (72)$$

which constitutes a set of uncoupled ordinary differential equations, where  $\mathbf{y}$  holds the modal displacements.

### 4.2. Modal Parameters

Resonance frequencies are derived under free vibration and are extracted from the eigenvalues using the ansatz  $y_i = e^{j\omega_i t}$ , where  $i$  is the mode index. The modal frequencies are then extracted by substitution into (72):

$$\omega_i = \sqrt{-Q_{i,i}}, \quad f_i = \frac{\omega_i}{2\pi}. \quad (73)$$

The column vector  $\mathbf{c}_E$  in (72) holds the input modal amplitudes, and the output torque in (69) can be re-written for the modal displacements  $\mathbf{y}$ :

$$T_P = \mathbf{h}_P^T \mathbf{Z}\mathbf{P}\mathbf{y}. \quad (74)$$

Using the substitution  $\mathbf{Z} = \mathbf{P}\mathbf{Q}\mathbf{P}^{-1}$  derives a column vector  $\mathbf{c}_P$  holding output modal amplitudes:

$$T_P = \mathbf{c}_P^T \mathbf{y}, \quad \mathbf{c}_P = \mathbf{Q}^T \mathbf{P}^T \mathbf{h}_P. \quad (75)$$

The modal amplitudes are then consolidated through element-by-element multiplication for an overall set corresponding to the resonance frequencies:

$$\mathbf{c} = \mathbf{c}_E \odot \mathbf{c}_P. \quad (76)$$

The transformation to a modal system provides direct access to parameters, allowing a selection of all modes below 20 kHz.

### 4.3. Frequency-Dependent Damping

While simple loss models have previously been incorporated into the helical spring equations [15], the lack of any extensive research regarding losses in the helical spring motivates a more freely-defined approach by directly imposing damping at this stage in a phenomenological manner. Imposing a quadratic dependency on frequency

$$\sigma_i = \sigma_2 \omega_i^2 + \sigma_0, \quad (77)$$

yields a reasonable approximation to experimental results, where  $\sigma_0$  and  $\sigma_2$  are damping constants.

#### 4.4. Temporal Discretisation

A sampling frequency  $f_s = 44.1$  kHz and subsequent time step  $\Delta_t = 1/f_s$  can now be introduced to simulate the modal system. Using the resonance frequencies, corresponding modal amplitudes, loss parameter, and time step a modal update equation is derived which preserves the mode frequencies and decay rates [3]:

$$y_i^{n+1} = a_i y_i^n + d_i y_i^{n-1} + c_i T_E^n, \quad (78)$$

where  $a_i = 2\epsilon_i \cos(\omega_i \Delta_t)$ ,  $d_i = -\epsilon_i^2$ , and  $\epsilon_i = e^{-\sigma_i \Delta_t}$ . The  $n$  superscript represents the sample index and the output for every sample is taken by summing all the modes for  $y^n$ .

#### 4.5. Simulated Spring Responses

The modal reverb algorithm in (78) is implemented for a steel spring using the values in Table 1, defined to simulate the measurement of a spring from the *Leem Pro KA-1210* [11].

Table 1: Simulation parameter values.

spring values		loss values		input/output values	
$\mu$	0.0389	$\sigma_0$	$3 \text{ s}^{-1}$	$\phi_E$	$80^\circ$
$b$	1.3	$\sigma_2$	$3 \times 10^{-9} \text{ s}$	$\phi_P$	$100^\circ$
$\lambda$	1901.7				

Firstly, the validity of the applied discretisation steps is examined in terms of the eigendecomposition results. Numerous simulations with different spring parameters have strictly yielded real-valued eigenvalues and eigenvectors, implying that the FD matrix  $\mathbf{Z}$  is unconditionally negative-definite. The found eigenvalues are systematically negative, thus — through (73) — the methodology guarantees real-valued modal frequencies. A more formal proof will require energy analysis, similar to that conducted in [12, 15], but now involving wider spatial stencils.

Secondly, the displacement mode shapes are examined. The mode shapes of  $v$  and  $w$  are directly extracted from the eigenvector matrix  $\mathbf{P}$  in (70). The mode shape for  $u$  is then recovered from the  $w$  mode shape using a numerical version of the aforementioned relationship  $u = \partial_s w$ . Figure 5 shows a small selection of displacement mode shapes with corresponding resonance frequencies. Comparisons to the relevant derivatives in the boundary conditions from Section 2.4 confirm that the boundary conditions are satisfied numerically for all three polarisations.

These findings suggest that the spatial discretisation, including the numerical boundary treatment, represents a robust step in the procedure for calculation of the modal parameters.

The simulated impulse response is shown in Figure 6, including a measured response for comparison. Audio files are available on the companion webpage.<sup>2</sup> The numerical model renders 2031 modes in the audio range, yielding a richer and more complex sound compared to audio examples from a simplified model [3]. Past research [19] has shown that this many modal oscillators can be implemented in real-time using vectorised instruction sets, e.g. AVX2, common in many modern CPU architectures.

Analysis of spectrograms shows that the modal algorithm captures the characteristics of a number of spring reverb features. The most prominent is the reproduction of the main series of dispersive echoes (referred to as chirps). The chirp shape, echo densities, and progressive temporal blurring from the measurement are

<sup>2</sup><http://www.socasites.qub.ac.uk/mvanwalstijn/dafx21a/>

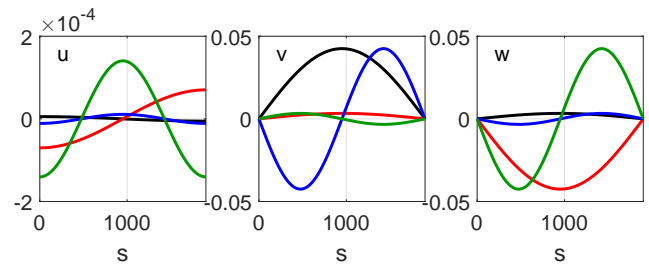


Figure 5: Displacement modal shapes of normal modes of low frequency/wavenumber. The corresponding modal frequencies are: —  $f_{11} = 21.1$  Hz; —  $f_{12} = 24.1$  Hz; —  $f_{17} = 42.3$  Hz; —  $f_{19} = 48.2$  Hz.

all captured. Two transition frequencies are accurately reproduced around 4 kHz, reflecting the behaviour of the two curves that appear in the dispersion relation in Figure 4. The higher coherency of the chirps in the upper frequency region is also well reproduced in the simulation, with their increased structure and lower echo density apparent. The dip in the spectrogram situated around 1 kHz corresponds to the third lower transition frequency represented by a grey dotted line in Figure 4.

As can be seen from the plots, there are a number of discrepancies between the modelled and the measured response. The amplitude envelope clearly differs, with the modelled response not having a smooth roll-off and having an increased amplitude at the transition frequencies. These are likely due to the omission of magnetic beads, and employing modal amplitude manipulations (similar to [3]) enables a closer visual and aural match to the measurement, as shown in the middle of Figure 6.

However, some issues are not accounted for by such modal manipulations. The coherent echoes visible above the transition frequency extend to the lower region, whereas they are far less present in the measurement. Informal listening tests confirm that these discrepancies are perceptually prominent, and are difficult to correct for by manipulation of modal amplitudes. Also, there are multiple sets of main chirps in the model that are not visible in the measurement.

## 5. CONCLUSIONS

A modal spring reverb formulation based on the thin helical spring model has been developed. The novelty of the work resides in how the methodology differs from previous studies: the discretisation approach, compared to [3], now only discretises the spatial domain which improves the overall accuracy of the numerical model; compared to [15], the excitation and pick-up are formulated as embedded reciprocal mechanisms; a specific set of lossless boundary conditions in the reduced model variables  $v$  and  $w$  is presented; least-squares based optimal FD coefficients are employed, yielding high accuracy in the dispersion relation over a larger wavenumber range than Taylor-series derived coefficients, as such achieving comparable discretisation accuracy with a smaller number of grid nodes.

Comparison with a measured impulse response has indicated that several response features are reproduced. However, the presented model is not easily configured to predict correct modal amplitudes (and possibly, phases), which is likely due to the simplified excitation and pick-up mechanisms. Hence, as also alluded

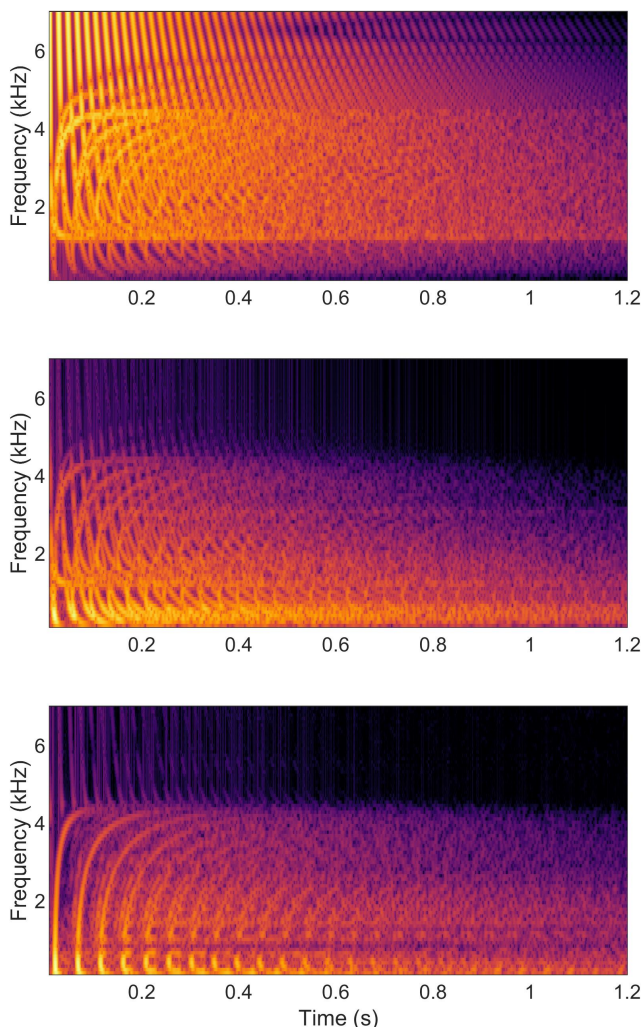


Figure 6: Impulse response comparisons using optimised FD coefficients with  $K = 5$  and  $M = 1100$ . Top: Simulated response. Middle: Simulated response with modal manipulations. Bottom: measured response [11].

to in [14, 15], obtaining a closer match will require modelling the coupling of the magnets to the helical spring. The prospect of extending the model in that manner has in fact motivated the numerical approach taken here. That is, while the eigenvalue problem of the isolated spring system could probably also be addressed with analytical methods (e.g. using separation of variables), similar analytic treatment of an extended system incorporating the bead coupling would present significant new challenges. The authors' current expectation is that, provided that a suitable linear 3-D coupling mechanism can be formulated, the numerical approach taken in this paper can be more easily extended in that regard.

## 6. REFERENCES

- [1] L. Hammond, "Electrical musical instrument," US Patent No. 2230836, 1941.
- [2] A. C. Young, "Artificial reverberation unit," US Patent No. 3106610, 1961.
- [3] M. van Walstijn, "Numerical calculation of modal spring reverb parameters," in *Proc. of 23rd Int. Conf. of Digital Audio Effects (DAFx2020)*, 2020, pp. 38–45.
- [4] V. Välimäki, J. Parker, and J. S. Abel, "Parametric spring reverberation effect," *Journal of the AES*, vol. 58, no. 7/8, pp. 547–562, 2010.
- [5] J. S. Abel, D. P. Berners, S. Costello, and J. O. Smith III, "Spring reverb emulation using dispersive allpass filters in a waveguide structure," in *Proc. of 121st AES Convention*, 2006.
- [6] J. Parker, "Efficient dispersion generation structures for spring reverb emulation," *EURASIP Journal on Advances in Signal Processing*, 2011.
- [7] H. Gamper, J. Parker, and V. Välimäki, "Automated calibration of a parametric spring reverb model," in *Proc. of 14th Int. Conf. on Digital Audio Effects (DAFx-11)*, 2011, pp. 416–421.
- [8] J. S. Abel, S. A. Coffin, and K. S. Spratt, "A modal architecture for artificial reverberation with application to room acoustics modeling," in *Proc. of 137th AES Convention*, 2014.
- [9] J. S. Abel and E. K. Canfield-Dafilou, "Dispersive delay and comb filters using a modal structure," *IEEE Signal Processing Letters*, vol. 26, no. 12, pp. 1748–1752, 2019.
- [10] T. Tarnopolskaya and F. de Hoog, "Asymptotic analysis of the free in-plane vibrations of beams with arbitrarily varying curvature and cross-section," *Journal of Sound and Vibration*, vol. 196, no. 5, pp. 659–680, 1996.
- [11] J. Parker and S. Bilbao, "Spring reverberation: A physical perspective," in *Proc. of 12th Int. Conf. on Digital Audio Effects (DAFx-09)*, 2009, pp. 416–421.
- [12] S. Bilbao and J. Parker, "A virtual model of spring reverberation," *IEEE Trans. on Audio, Speech, and Language Processing*, vol. 18, no. 4, pp. 799–808, 2010.
- [13] W. H. Wittrick, "On elastic wave propagation in helical springs," *Int. Journal of Mechanical Sciences*, vol. 8, no. 1, pp. 25–47, 1966.
- [14] S. Bilbao and J. Parker, "Perceptual and numerical aspects of spring reverberation modeling," in *Proc. of 20th Int. Symp. on Music Acoustics*, 2010.
- [15] S. Bilbao, "Numerical simulation of spring reverberation," in *Proc. of 16th Int. Conf. of Digital Audio Effects (DAFx-13)*, 2013.
- [16] S. Mazumder, *Numerical Methods for Partial Differential Equations*, Academic Press, Elsevier, 2016.
- [17] B. Fornberg, "Generation of finite difference formulas on arbitrarily spaced grids," *Mathematics of Computation*, vol. 51, no. 184, pp. 699–706, 1988.
- [18] S. K. Lele, "Compact finite difference schemes with spectral-like resolution," *Journal of Computational Physics*, vol. 103, no. 1, pp. 16–42, 1992.
- [19] M. van Walstijn and S. Mehes, "An explorative string-bridge-plate model with tunable parameters," in *Proc. of 20th Int. Conf. of Digital Audio Effects (DAFx-17)*, 2017, pp. 291–298.